

Integrated dopamine sensing and 40 Hz hippocampal stimulation improves cognitive performance in Alzheimer's mouse models

Received: 5 June 2024

Accepted: 4 June 2025

Published online: 01 July 2025


 Check for updates

Shiya Lv^{1,2}, Fan Mo^{1,2}, Zhaojie Xu^{1,2}, Yu Wang^{1,2}, Yaoyao Liu^{1,2}, Meiqi Han^{1,2}, Yiming Duan^{1,2}, Luyi Jing^{1,2}, Fanli Kong^{1,2}, Qianli Jia^{1,2}, Ming Li^{1,2}, Wei Xu^{1,2}, Peiyao Jiao^{1,2}, Mixia Wang^{1,2}, Juntao Liu^{1,2}, Jinping Luo^{1,2}, Junbo Wang^{1,2}, Zhongwei Fan^{1,2}, Yilin Song^{1,2} , Yirong Wu^{1,2}  & Xinxia Cai ^{1,2} 

Hippocampal degeneration and reduced dopamine levels in Alzheimer's disease are associated with severe memory and cognitive impairments. However, the lack of multifunctional in situ neural chips has posed challenges for integrated investigations of Alzheimer's disease pathophysiology, dopamine dynamics, and neural activity. Therefore, we developed NeuroRevive-Flex-Chip, a flexible neural interface capable of precise electrical modulation and simultaneous in situ monitoring of dopamine levels and neural activity. In this study, the NeuroRevive-FlexChip demonstrates improved electrochemical detection sensitivity and modulation efficiency. Preliminary observations in APP/PS1 mice indicate that implantation of the chip in the hippocampal CA1 region, combined with 40 Hz stimulation, may contribute to the restoration of dopamine release, a reduction in neuronal hyper-synchronization, and a shift toward more stable firing patterns. These effects appear to be modulated by dopamine-related mechanisms. Furthermore, 40 Hz stimulation was observed to correlate with reduction in A β ₄₂ deposition and modest improvements in spatial cognition performance, as assessed by the Y-maze test. These findings highlight the potential of NeuroRevive-FlexChip as a research tool for investigating the mechanisms of 40 Hz stimulation in Alzheimer's disease models. Further studies could explore its utility in clarifying the relationship between dopamine dysfunction, neural activity, and amyloid pathology. While these early results are promising, additional preclinical and translational research will be necessary to assess the therapeutic potential of this approach for neurodegenerative diseases.

In Alzheimer's disease (AD) models, the CA1 region pathway in the hippocampus^{1–3} shows significant structural and functional alterations that correlate with cognitive and memory impairments⁴. One major cause is the formation and accumulation of beta-amyloid oligomers⁵, which disrupt the internal structure of neurons⁶, causing

neuron loss⁷, synaptic degeneration⁸, and neuronal dysfunction⁹. These pathological changes are also associated with disturbances in the dopaminergic system and reduced dopamine (DA) levels^{10–12}, potentially influencing the cognitive, motor and behavioral symptoms observed in AD^{13–15}. The complex interplay between DA

¹State Key Laboratory of Transducer Technology, Aerospace Information Research Institute, Chinese Academy of Sciences, Beijing 100190, China. ²University of Chinese Academy of Sciences, Beijing 100049, China.  e-mail: ylsong@mail.ie.ac.cn; wyr@mail.ie.ac.cn; xxcai@mail.ie.ac.cn

signaling and neural activity may provide important insights into AD pathogenesis at molecular and cellular levels. However, technical limitations in simultaneously monitoring these dynamic processes have constrained our understanding of their precise relationships. Further investigation of these mechanisms could help identify research directions for AD intervention strategies.

Electrical stimulation (ES) technologies, such as deep brain stimulation (DBS)^{16–19}, transcranial electrical stimulation (TES)^{20,21}, and transcranial magnetic stimulation (TMS)²², emerge as potential methods to activate neural networks and enhance neurotransmitter DA transmission²², aiming to improve memory accuracy in AD patients^{23,24}. Although DBS, TES, and TMS offer targeted control, they still cannot provide real-time feedback on the effects of ES on the release of electrochemical neurotransmitters and neuronal electrophysiological activity. Therefore, the development of a tool tailored to the hippocampus, capable of concurrently monitoring DA levels, neuronal activity, and in-situ electrical modulation of dopaminergic neurons, is urgently required.

Presently, similar neural chips typically offer only single-function detection or regulation capabilities^{25,26}. And most rely on rigid substrate materials^{27,28}. However, due to their brittleness and thickness, the rigid substrates differ markedly in Young's modulus from brain tissue (nearly 10^6), potentially causing significant relative motion injuries during long-term implantation²⁹. In contrast, using flexible materials like parylene with a lower Young's modulus as the substrate can significantly reduce damage to surrounding neurons and better preserve complete neural information³⁰.

In this work, we develop the NeuroRevive-FlexChip, a versatile and flexible neural chip designed to concurrently monitor DA levels and neuro-electrophysiological activity while regulating in-situ ES. The NeuroRevive-FlexChip incorporates specialized coatings: PtNPs/PEDOT/PPy/MWCNTs for ES and PtNPs/PEDOT/MWCNTs for neurophysiological and electrochemical detection. These tailored modifications ensure optimal accuracy, cost-effectiveness, and manufacturing efficiency. Further, our simulation analyses post-implantation in mouse brains demonstrate that the NeuroRevive-FlexChip's design minimizes detection interference. Using a 40 Hz stimulation frequency with variable stimulation currents, we observed a short-term rebooting phenomenon in DA release following ES. During this rebooting phase, an increase in DA levels correlates with burst firing in neurons, while a decrease corresponds to tonic firing. At the macro-behavioral level, 40 Hz ES enhances the spontaneous alternation accuracy in the Y-maze. At the microscopic neural molecular and cellular level, a reduction in $\text{A}\beta_{42}$ and changes in the microglial cell morphology are observed. Overall, the development of the NeuroRevive-FlexChip integrates electrophysiological and electrochemical dual-modalities with ES in a single device, offering new possibilities for alleviating early symptoms of AD and laying the groundwork for a deeper understanding of DA release in the hippocampus in the context of AD.

Results

Structure of the Neurorevive-FlexChip

Structurally, the NeuroRevive-FlexChips utilize a dual-conductive layer design, targeting the CA1 region pathway with high throughput (Fig. 1a, b). The fabrication process is described in Fig. 1c. The NeuroRevive-FlexChips functionally facilitate in situ electrophysiological signals and DA concentration detection during ES modulation.

The NeuroRevive-FlexChips feature a dual concentric ring setup for ES. The 500 μm outer ring functions as the positive electrode, and the 420 μm inner ring is grounded (Fig. 1a, b). The formation of an inner grounding shield effectively mitigates the crosstalk between voltage induced by ES and the target electrochemical signals (Fig. 1d, e). Regarding spatial resolution, the NeuroRevive-FlexChips provide two levels scales: 20 μm and 10 μm microelectrodes. The

20 μm microelectrodes are positioned on the outer side to initially identify the target neural network's activity patterns. The 10 μm microelectrodes, located on the inner side, enable detailed detection and improved spatial resolution after establishing the basic firing patterns of the neural network. The dual-resolution approach ensures accurate detection while enhancing the precision of the measurements.

The electrical performance of the Neurorevive-FlexChip

The detection performance and ES capabilities of four electrode surface materials—Bare, PtNPs, PtNPs/PPy/MWCNTs, PtNPs/PEDOT:PSS/MWCNTs, and PtNPs/PEDOT:PSS/PPy/MWCNTs—were evaluated (Figure. S1–S3). At 1 kHz, the impedance values for 20 μm microelectrodes are recorded as 30 M Ω , 59 k Ω , 122 k Ω , 2 k Ω , and 3 k Ω respectively (Fig. 2a, c), with corresponding phase delays of 82°, 37°, 23°, 4°, and 7° (Fig. 2b, c). The impedance analysis reveals that PtNPs significantly reduce impedance, while further additions like PPy/MWCNTs do not continue this trend. Both PtNPs/PEDOT:PSS/MWCNTs and PtNPs/PEDOT:PSS/PPy/MWCNTs modified electrodes lower the impedance by more than four orders of magnitude compared to the bare microelectrode. The phase delay decreases dramatically for the modified surfaces, resulting in reductions ranging from 55% to 95% compared to the bare microelectrode (Fig. 2c). The FlexChip detects the Signal-to-Noise Ratio (SNR) with a minimum noise baseline of 20 μV and a maximum noise baseline of 30 μV , achieving an SNR > 5 (Figure. S4).

Scanning electron microscopy (SEM) images illustrate the surface structures of modified microelectrodes (Fig. 2d–f). The characteristics of these materials closely influence the changes in impedance. PtNPs create nano-flower structures that significantly increase the surface area. MWCNTs and PEDOT:PSS enhance biocompatibility and further reduce impedance and phase delay after PtNPs modification. Despite PPy's minimal content, it fills the nano-flower structures' pores, which increases electrode impedance.

The ES efficiency of three NeuroRevive-FlexChip modifications PtNPs/PPy/MWCNTs, PtNPs/PEDOT:PSS/MWCNTs, and PtNPs/PEDOT:PSS/PPy/MWCNTs was evaluated. Cyclic voltammetry (CV) scans across a range of -0.5 V to 0.5 V at varying currents (20 μA , 40 μA , 60 μA , 80 μA , 100 μA) were conducted on the microelectrodes (Fig. 2g–j). With increasing scan current, the CV curve areas enlarged. Calculating the double-layer capacitance via the formula (2), the PtNPs/PPy/MWCNTs and PtNPs/PEDOT:PSS/MWCNTs modifications exhibited capacitances of $0.09 \pm 0.01\ \mu\text{F}$ and $0.64 \pm 0.03\ \mu\text{F}$, respectively. The PtNPs/PEDOT:PSS/PPy/MWCNTs modified electrode demonstrated the highest capacitance at $1.81 \pm 0.14\ \mu\text{F}$, showing a strong linear correlation ($R^2 = 0.99$). PtNPs/PEDOT:PSS/PPy/MWCNTs modified electrode exhibited a double-layer capacitance 20 times higher than that of PtNPs/PPy/MWCNTs and 2.8 times higher than PtNPs/PEDOT:PSS/MWCNTs (Fig. 2k).

Additionally, charge storage capacity assessments revealed values of $0.24 \pm 0.05\ \text{mC}\cdot\text{cm}^{-2}$ for PtNPs/PPy/MWCNTs, $1.4 \pm 0.35\ \text{mC}\cdot\text{cm}^{-2}$ for PtNPs/PEDOT:PSS/MWCNTs, and $2.97 \pm 0.78\ \text{mC}\cdot\text{cm}^{-2}$ for PtNPs/PEDOT:PSS/PPy/MWCNTs. Consequently, the PtNPs/PEDOT:PSS/PPy/MWCNTs modified electrode showcased a charge storage capacity 12.4 times greater than PtNPs/PPy/MWCNTs and 2.12 times greater than PtNPs/PEDOT:PSS/MWCNTs (Fig. 2l).

In conclusion, the PtNPs/PEDOT:PSS/MWCNTs modified electrode offers superior detection and the PtNPs/PEDOT:PSS/PPy/MWCNTs offers superior stimulation performance, making it the preferred choice for minimizing microelectrode corrosion and tissue damage.

The dopamine detection performance of the neurorevive-FlexChip

In phosphate-buffered saline (PBS), the microelectrode displays no oxidation peaks, whereas in a 200 mM DA solution, an oxidation

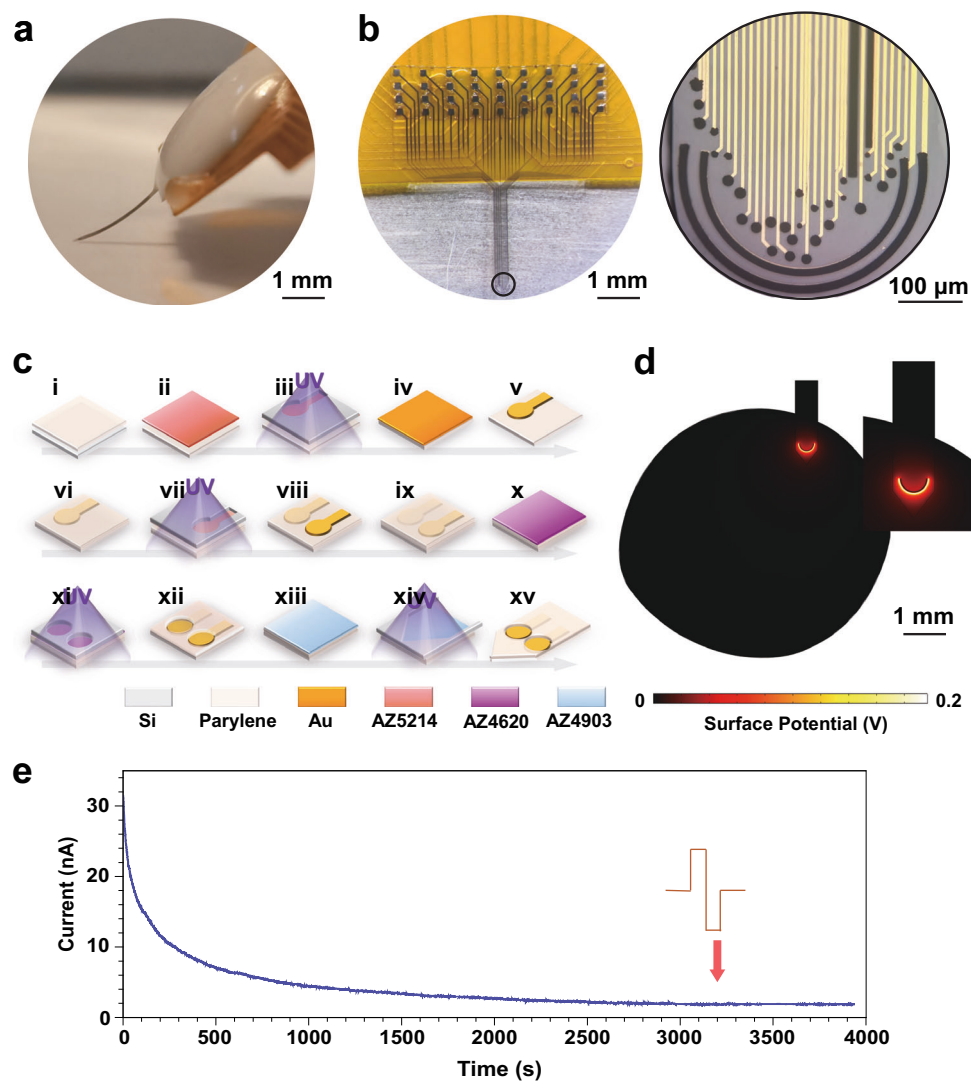


Fig. 1 | The neurorevive-FlexChip. **a** Completed Packaging of NeuroRevive-FlexChip (scale bars: 1 mm). **b** Full View of NeuroRevive-FlexChip (scale bars: 1 mm), and detailed image of the tip of the mfMEA in the black circle (scale bars: 100 μm). **c** The NeuroRevive-FlexChip fabrication process: i Deposition of a 6 μm parylene layer onto a cleaned silicon wafer; ii Spin-coating of photoresist AZ5214 onto the parylene layer; iii Photolithographic definition of patterns for the deep conductive layer; iv–v Sputtering and lift-off of the deep Cr/Au (30/200 nm) conductive layer; vi Deposition of a 2 μm parylene layer; vii Photolithographic definition of patterns

for the shallow conductive layer; viii Sputtering and lift-off of the shallow Cr/Au (30/200 nm) conductive layer; ix Deposition of another 2 μm parylene layer; x Spin-coating of photoresist AZ4620 onto the parylene layer; xi–xii Exposure of microelectrodes and pads through photolithography and etching; xiii Spin-coating of photoresist AZ4903 onto the parylene layer; xiv–xv Patterning of the NeuroRevive-FlexChip contours through photolithography and etching. **d** Surface Potential Simulation from Electrical Stimulation (ES) (scale bars: 1 mm). **e** The electrochemical response under in vitro stimulation.

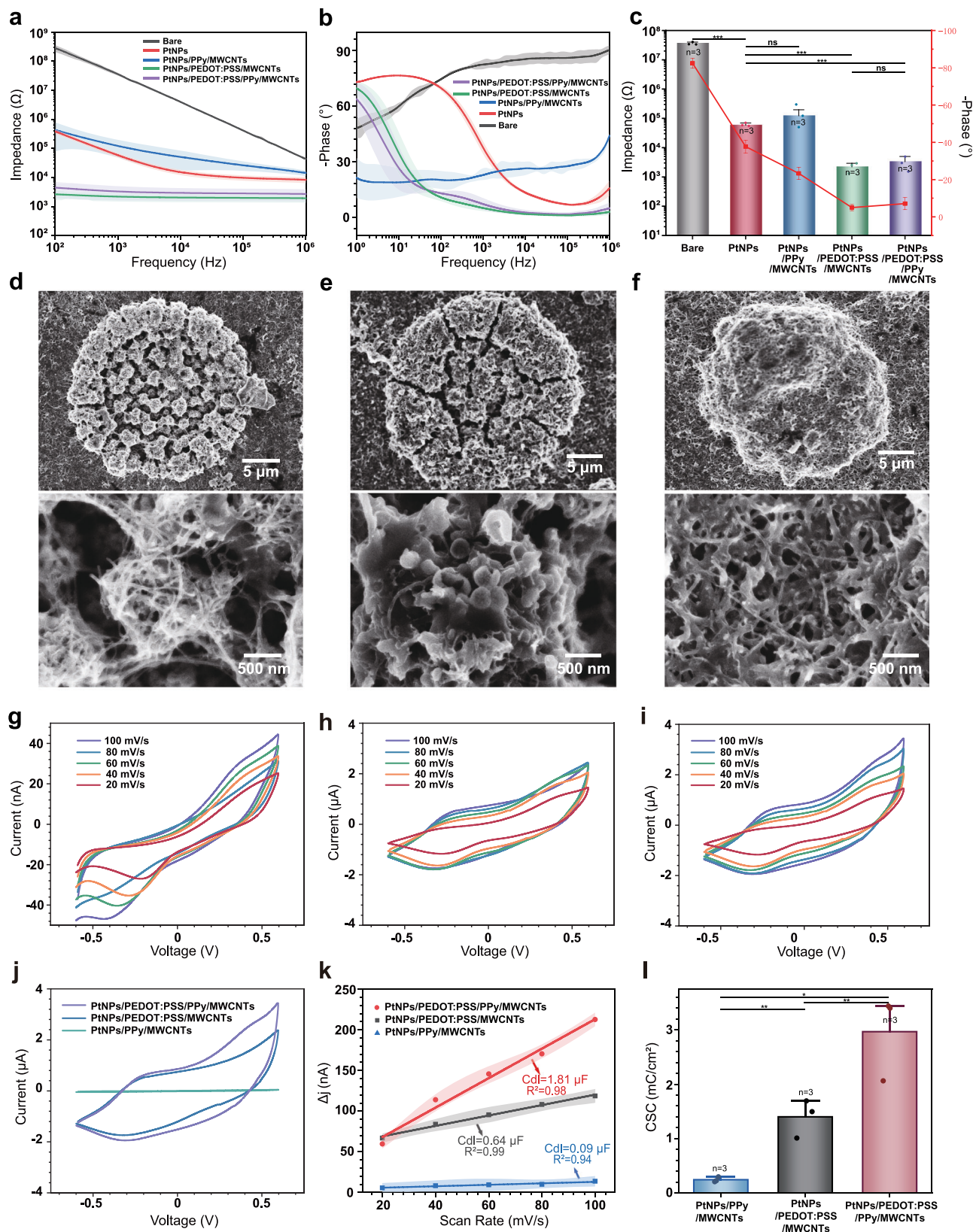
peak emerges at 0.36 V (Fig. 3a). Therefore, the microelectrodes concentration-response curve to DA is calibrated at a voltage of 0.36 V (Fig. 3b, c), covering a DA concentration range from 0.01 to 80 μM . A distinct step response in the microelectrode feedback current is observed at 0.1 μM DA. The current noise is primarily caused by thermal noise, environmental noise, and intrinsic device noise, with a baseline of 1.5 nA (Fig. 3c). Below 10 μM , the current fitting curve exhibits a slope of $0.03 (\pm 0.002)$, an intercept of $2.06 (\pm 0.08)$, and a linear correlation coefficient (R^2) of 0.99. Above 10 μM , the slope increases to $0.07 (\pm 0.004)$, with an intercept of $1.53 (\pm 0.02)$ and an R^2 of 0.97. The microelectrode exhibits sensitivities of 71.71 pA/ μM at low concentrations, 31.04 pA/ μM at high concentrations, with an overall sensitivity of 37.54 pA/ μM across the full range. (Fig. 3d).

The specificity of the microelectrode is further assessed by introducing potential interferents: uric acid (UA), lactic acid (LA),

ascorbic acid (AA), and 5-hydroxytryptamine (5-HT), each at 10 μM , into the PBS solution (Fig. 3e). Against a 5 μM and 10 μM DA target, the microelectrode shows a 100% response to DA, negligible response to UA, LA, and 5-HT, and a 10% response to AA, affirming its high specificity for DA detection (Fig. 3f).

40 Hz ES-induced dopamine reboot and hyper-synchronization quelling in mice

The current variations on the electrochemical detection microelectrodes of the NeuroRevive-FlexChips indicate fluctuations in DA concentration (Fig. 4a). Once ES starts, DA release increases regardless of the current's intensity. However, DA release reaches a peak and then decreases, influenced by factors like synthesis rate, reuptake, and metabolism^{31,32}. This decline occurs regardless of ongoing stimulation. After stimulation ends, DA release trends toward its pre-stimulation levels and may show a secondary rise. This phenomenon could potentially be linked to



mechanisms such as rho-mediated internalization of DA transporters, though further investigation is required to clarify the underlying processes³³. Each stimulation session appears to be followed by a recurring pattern in DA concentration dynamics, including an initial decrease, a subsequent rise, and a later decline (Fig. 4b). After 100 μA and 200 μA stimulation, the initial valley of DA gradually increases. At 300 μA ,

the initial valley significantly increases, nearly tripling. Following 300 μA stimulation, a trend toward elevated DA levels in the initial and subsequent valleys was observed, though further studies are needed to assess the stability and reproducibility of this effect.

The pre-ES average spike firing rate in awake APP/PS1 mice was 4.79 Hz, almost six times the 0.84 Hz in wild-type mice. The

Fig. 2 | The electrical performance of the neurorevive-FlexChip. **a–c** Impedance and phase of NeuroRevive-FlexChip with the following conditions: bare surface, surface modified with PtNPs, PtNPs/PPy/MWCNTs, PtNPs/PEDOT:PSS/MWCNTs, and PtNPs/PEDOT:PSS/PPy/MWCNTs ($n = 3$ independent detection sites per group; data are presented as mean \pm s.d.; P values: Bare vs. PtNPs, $P = 0.0001$; PtNPs vs. PtNPs/PPy/MWCNTs, $P = 0.1792$; PtNPs vs. PtNPs/PEDOT:PSS/MWCNTs, $P = 0.0008$; PtNPs vs. PtNPs/PEDOT:PSS/MWCNTs/PPy, $P = 0.0009$; PtNPs/PEDOT:PSS/MWCNTs vs. PtNPs/PEDOT:PSS/MWCNTs/PPy, $P = 0.332$). **d–f** SEM image of NeuroRevive-FlexChip with the following conditions: surface modified with PtNPs/PPy/MWCNTs, PtNPs/PEDOT:PSS/MWCNTs, and PtNPs/PEDOT:PSS/PPy/MWCNTs. **g–i** The CV curves of modified micro-electrodes of NeuroRevive-FlexChip. **g** PtNPs/PPy/MWCNTs, **h** PtNPs/PEDOT:PSS/MWCNTs, and **i** PtNPs/PEDOT:PSS/PPy/MWCNTs. **j** The CV scanning (0.2–0.6 V) in a 200 μ M DA solution of the NeuroRevive-

FlexChip. **k** The double layer capacitance (C_{dl}) of the PtNPs/PPy/MWCNTs, PtNPs/PEDOT:PSS/MWCNTs and PtNPs/PEDOT:PSS/PPy/MWCNTs modified micro-electrodes of NeuroRevive-FlexChip ($n = 3$ independent detection sites per group; data are presented as mean \pm s.d.). **l** The charge storage capacity of the PtNPs/PPy/MWCNTs, PtNPs/PEDOT:PSS/MWCNTs and PtNPs/PEDOT:PSS/PPy/MWCNTs modified micro-electrodes of NeuroRevive-FlexChip ($n = 3$ independent detection sites per group; data are presented as mean \pm s.d.; P values: PtNPs/PPy/MWCNTs vs. PtNPs/PEDOT:PSS/MWCNTs, $P = 0.0048$; PtNPs/PEDOT:PSS/MWCNTs vs. PtNPs/PEDOT:PSS/PPy/MWCNTs, $P = 0.0344$; PtNPs/PPy/MWCNTs vs. PtNPs/PEDOT:PSS/PPy/MWCNTs, $P = 0.0039$). Statistical significance was assessed by unpaired two-tailed Student's t -tests. ns, not significant ($p \geq 0.05$); * $p < 0.05$, ** $p < 0.01$, *** $p < 0.001$, **** $p < 0.0001$.

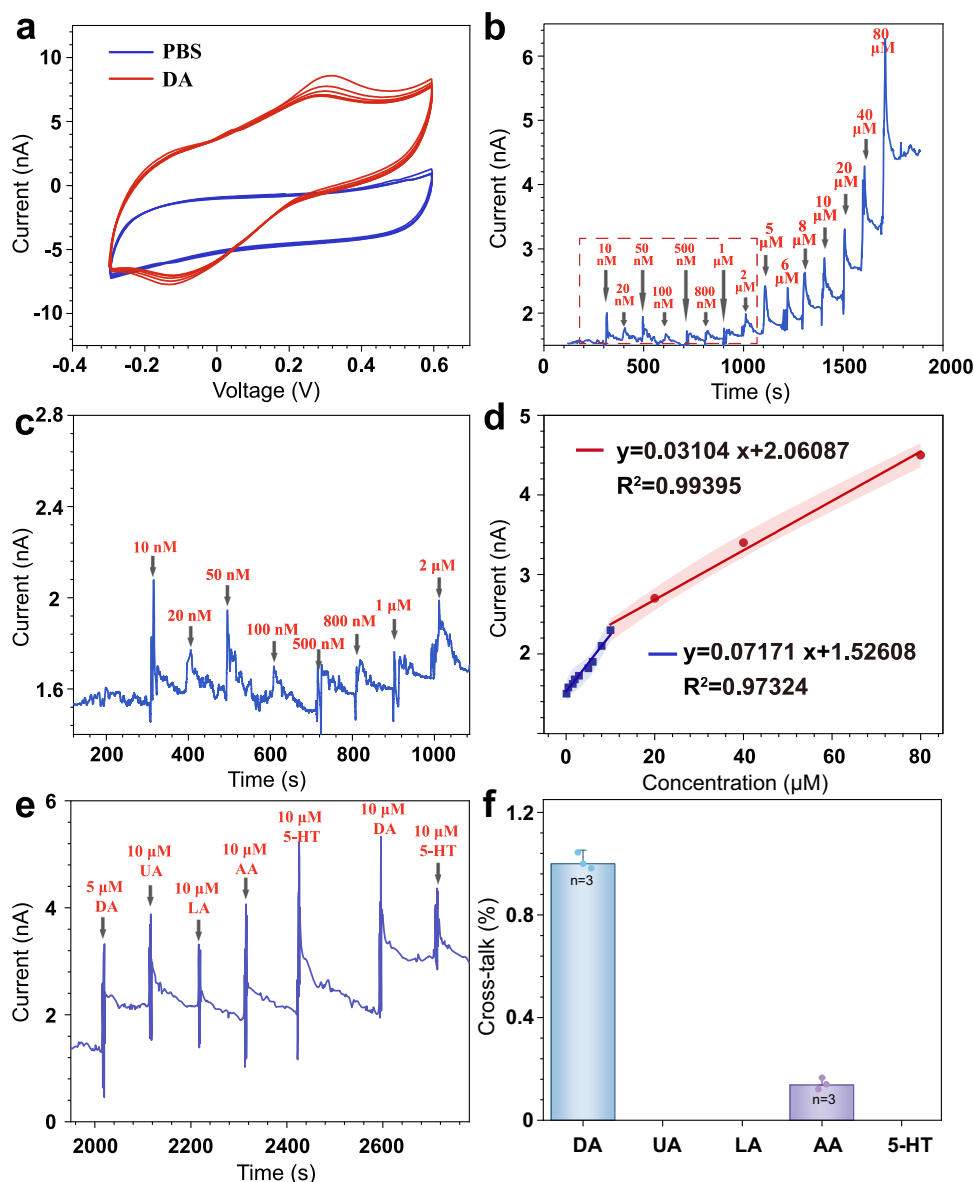


Fig. 3 | The dopamine (DA) detection performance of the NeuroRevive-FlexChip. **a** Cyclic voltammograms of the NeuroRevive-FlexChip working micro-electrode in PBS and 200 μ M DA solution ($-0.3 - 0.6$ V, 100 mV/s). **b** Calibration curve of the DA detection micro-electrode (10 nM–80 μ M) (The red dashed box indicates the DA detection range of 10 nM–2 μ M, which is magnified in Fig. 3c.). **c** Local calibration curve of the DA detection microelectrode (10 nM–2 μ M). **d** Current response fitting curves at different DA concentrations (0–10 μ M):

$y = 0.07171x + 1.52608$, $R^2 = 0.973$; 10–80 μ M: $y = 0.03104x + 2.06087$, $R^2 = 0.994$) ($n = 3$ independent detection sites per group; data are presented as mean \pm s.d.). **e** Current response curves under the interference of UA, LA, AA, 5-HT. **f** Comparative current responses under interference ($n = 3$ independent detection sites per group; data are presented as mean \pm s.d.). Statistical significance was assessed by unpaired two-tailed Student's t -tests. ns, not significant ($p \geq 0.05$); * $p < 0.05$, ** $p < 0.01$, *** $p < 0.001$, **** $p < 0.0001$.

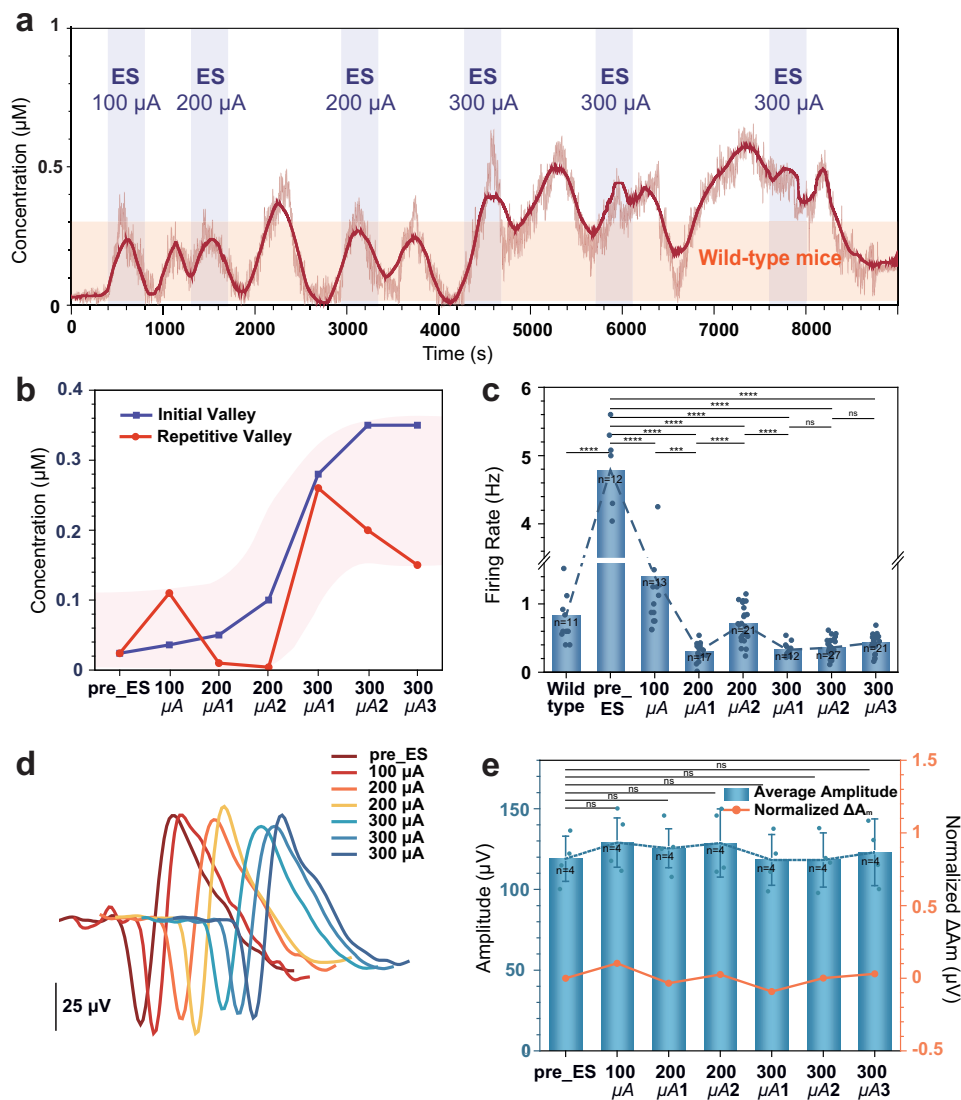


Fig. 4 | Electrical stimulation (ES) is rebooting DA and quelling hyper-synchronization firings. **a** Changes in DA concentration after each ES in AD mice (once at 100 µA; twice at 200 µA; thrice at 300 µA). **b** DA concentration in AD mice from the initial valley (the first concentration nadir observed after stimulation cessation) after ES to the repetitive valley after DA reboot (the nadir of DA concentration following spontaneous reboot and decline in the absence of electrical stimulation). **c** Spike firing rate in wild-type mice and AD mice pre and post each ES ($n = 20$ independent micro-electrode site; data are presented as mean \pm s.d.; P values: wild-type vs. Pre-ES, $P < 0.0001$; Pre-ES vs. 100 µA, $P < 0.0001$; Pre-ES vs. 200 µA, $P < 0.0001$; Pre-ES vs. 200 µA, $P < 0.0001$; Pre-ES vs. 300 µA, $P < 0.0001$; Pre-

ES vs. 300 µA, $P < 0.0001$; Pre-ES vs. 300 µA, $P < 0.0001$; 100 µA vs. 200 µA, $P = 0.0004$; 100 µA vs. 200 µA, $P < 0.0001$; 200 µA vs. 300 µA, $P < 0.0001$; 300 µA vs. 300 µA, $P = 0.4424$; 300 µA vs. 300 µA, $P = 0.0671$). **d** Mean action potential in AD mice pre and post each ES ($n = 20$ independent micro-electrode site; data are presented as mean \pm s.d.; P values: Pre-ES vs. 100 µA, $P = 0.4352$; Pre-ES vs. 200 µA, $P = 0.5646$; Pre-ES vs. 200 µA, $P = 0.4913$; Pre-ES vs. 300 µA, $P = 0.9491$; Pre-ES vs. 300 µA, $P = 0.9508$; Pre-ES vs. 300 µA, $P = 0.7707$). Statistical significance was assessed by unpaired two-tailed Student's t -tests. ns, not significant ($p \geq 0.05$); * $p < 0.05$, ** $p < 0.01$, *** $p < 0.001$, **** $p < 0.0001$.

elevated firing rate suggests a predisposition for early hyper-synchronization firings in APP/PS1 mice^{34–36}. Post-ES, a marked decrease in average firing rate was observed across sessions, with reductions ranging from approximately 70% to 94%, depending on the stimulation intensity and session. (Fig. 4c). On the contrary, spike amplitude variations remained within 15% (Fig. 4d, e). Following the initial 100 µA stimulation, spike amplitude increased by approximately 10%, whereas it decreased by 3% and 9% after the first 200 µA and 300 µA stimulations, respectively (Fig. 4e). Repeated stimulations at a single frequency appeared to elevate spike amplitude relative to baseline, although the physiological relevance of these amplitude fluctuations remains to be determined.

In summary, our data suggest that intermittent short-term ES via the NeuroRevive-FlexChip may influence DA release dynamics in a reproducible manner, meriting further mechanistic and translational exploration. Interestingly, APP/PS1 mice displayed elevated baseline neuronal firing rates suggestive of early hyper-synchronization³⁵. Following ES, firing rates decreased and approached levels observed in wild-type mice. However, further studies are needed to determine the long-term effects and potential therapeutic relevance of these changes.

Post-ES: profound interplay of DA fluctuations and spike activity
To further investigate the potential interplay between ES-associated changes in dopamine dynamics and the apparent reduction in hyper-

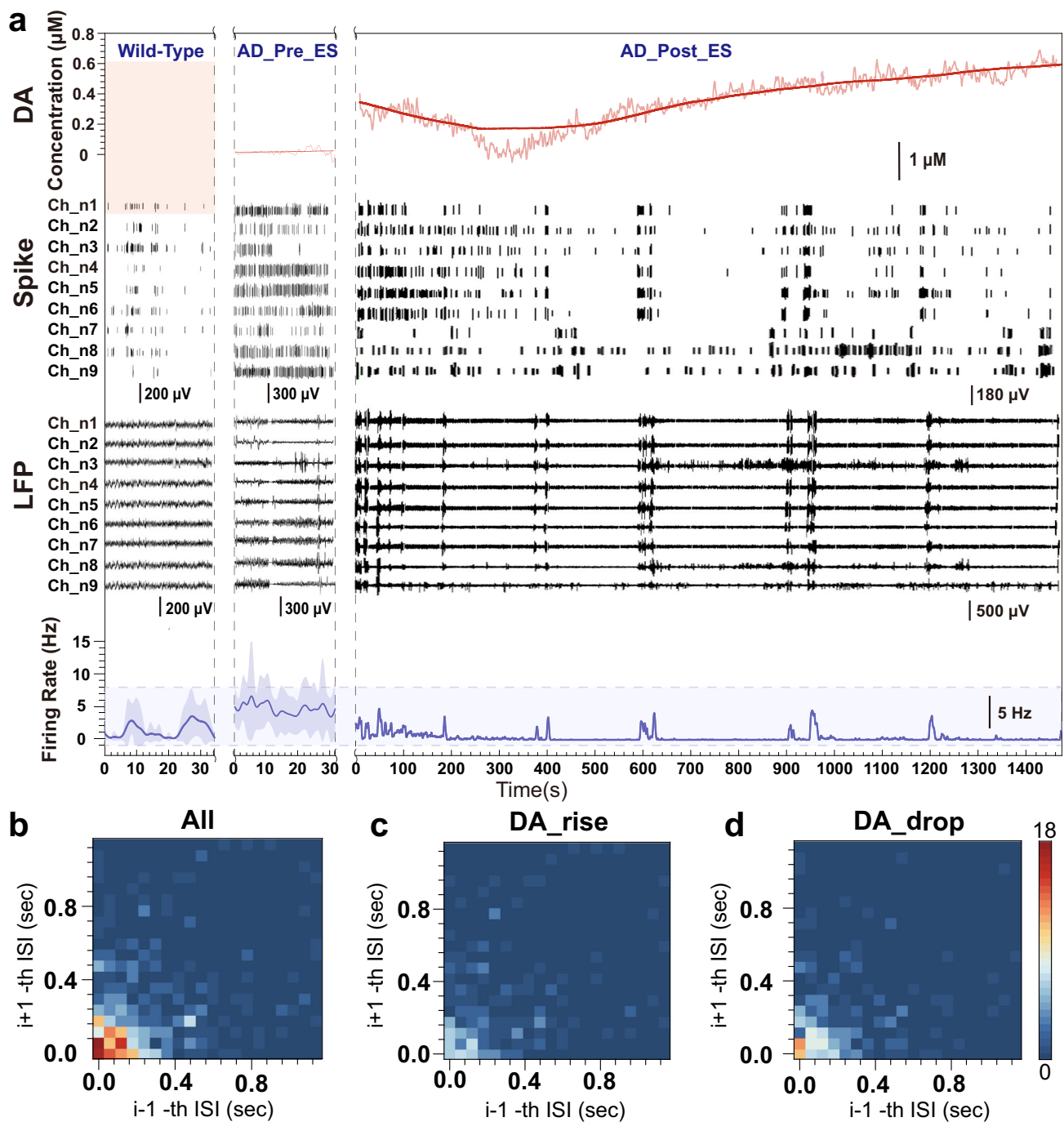


Fig. 5 | Post-ES: profound interplay of DA fluctuations and spike activity. **a** DA concentration, spike, LFP, and instantaneous spike firing rate in wild-type mice and AD mice pre- and post-ES. **b** Inter-spike interval (ISI) during the recording period after ES. **c** ISI corresponding to DA rise. **d** ISI corresponding to DA drop.

synchronized firings quelling post-ES in APP/PS1 mice, the DA fluctuations, spike, local field potential (LFP) electrophysiological signals, and the instantaneous spike rate histogram of wild-type mice, pre-ES APP/PS1 mice, and post 300 μA ES APP/PS1 mice were analyzed (Fig. 5a, S7).

Degeneration and dysfunction of VTA dopaminergic neurons observed in APP/PS1 mice and reported in neurodegenerative conditions—are associated with reduced dopaminergic outflow in the hippocampus^{11,37,38}. Initially, the DA concentration in the hippocampus of wild-type mice is approximately 0.14–1 μM ^{28,39}; however, the DA concentration in APP/PS1 mice is lower than that in wild-type mice (Figure. S8). In the short period after 300 μA ES,

DA concentration in APP/PS1 mice generally is higher, between 0.03–0.6 μM . Comparing the electrophysiological signals of wild-type mice and pre-stimulation APP/PS1 mice, APP/PS1 mice's spikes and LFP signals are denser, with the highest instantaneous spike firing rate in wild-type mice not exceeding 8 Hz. However, APP/PS1 mice show early hyper-synchronization firings, with rates reaching up to 15 Hz. Following stimulation, spikes and LFP signals in APP/PS1 mice appeared sparser, and the instantaneous spike firing rates decreased to values comparable to those observed in wild-type mice.

In post-ES APP/PS1 mice, at 200 s, a transition from decreasing to increasing DA concentration occurs. The timing of these changes

closely coincides with the transitions in spike patterns, transitioning from tonic firing to burst firing (Fig. 5a, and S10). However, the transitions between DA concentration and spike patterns exhibit a slight time lag (Fig. 5a). This slight time lag might reflect spatial separation between the recording electrodes, or possibly suggest a temporal relationship—though not necessarily causal—between neuronal firing and neurotransmitter release⁴⁰.

Further analysis of spike firing rate and burst rates. During the initial 200 s, with decreasing DA concentration, both spike firing and burst frequencies display peaks evenly distributed over time. Post-200 s, with rising DA concentration, the intervals between the burst widened. Most peak values for average spike firing rate fall within 2–6 Hz. Analysis distinguished the neuronal electrophysiological activities before and after the 200 s mark. The overall recording and Inter-Spike Interval (ISI) were examined before and after 200 s (Fig. 5b–d). During periods of decreasing DA concentration, a shorter ISI was observed (Fig. 5c). When DA concentration increased, there was a longer interval between high-frequency spike firings (Fig. 5d). This suggests a possible correlation between DA concentration and spike firing patterns: neurons exhibit tonic firings when DA concentration decreases and burst firing when DA concentration increases (Figure. S9).

In summary, post-ES microelectrophysiological observations suggest that hyper-synchronized firings observed in APP/PS1 mice may be reduced following ES. Moreover, when DA concentration increases, neuronal firing is characterized by burst firings; conversely, when DA concentration decreases, firing patterns tend to be tonic firings. Additionally, the average firing rate in each burst during DA rise was around 40.49 Hz, nearly identical to the stimulation frequency, raising future questions about the influence of stimulation frequency on burst synchrony.

Post-ES: Reduction in A β ₄₂ with Minimal Behavioral Effects

To elucidate the regulatory relationship between 40 Hz gamma oscillations and the dopaminergic system, we conducted targeted hippocampal microinjection experiments. Intracerebral administration of the non-selective DA receptor agonist apomorphine (APO, 10 μ M) induced an 8.5-fold increase in local DA concentration (from <100 nM to 850 nM) as measured by the NeuroRevive-FlexChip system, concomitant with a significant transition in neuronal firing patterns from baseline tonic firing to low-frequency burst firing (Figure. S10). These findings are consistent with established evidence demonstrating that DA receptor agonists may alleviate A β ₄₂-induced synaptic plasticity impairments and potentially contribute to reducing A β plaque burden through dual activation of D1/D2 receptor pathways^{41,42}. In antagonist intervention studies, administration of the selective D2 antagonist raclopride (5 μ M) did not significantly alter basal DA levels but completely abolished 40 Hz stimulation-induced DA release, with electrophysiological recordings confirming maintained tonic firing patterns. These results corroborate published findings that D1 receptor antagonism by SCH23390 eliminates the neuroprotective effects of cholinesterase inhibitors, while postmortem studies revealing substantial dopaminergic neuron loss (30–40%) in the substantia nigra pars compacta of Evidence from postmortem studies in Alzheimer's patients supports the hypothesis that dopamine system impairment may play a role in early disease progression¹¹.

To further investigate the effects of 40 Hz ES on the behavior of APP/PS1 mice, the Y-maze, a common behavioral test for spatial cognition in AD mice, was used (Fig. 6a). The correct entry into different arms of the maze by the mice during spontaneous alternation was considered correct. The spontaneous alternation rate increased from 47% (pre-ES) to 61% (post-ES) in APP/PS1 mice. In contrast, the spontaneous alternation rate of wild-type mice was 63% (Fig. 6b). Notably, 40 Hz ES was associated with an increased spontaneous alternation rate in APP/PS1 mice. While preliminary, this observation may suggest

a potential modulatory effect on spatial cognition that warrants further investigation.

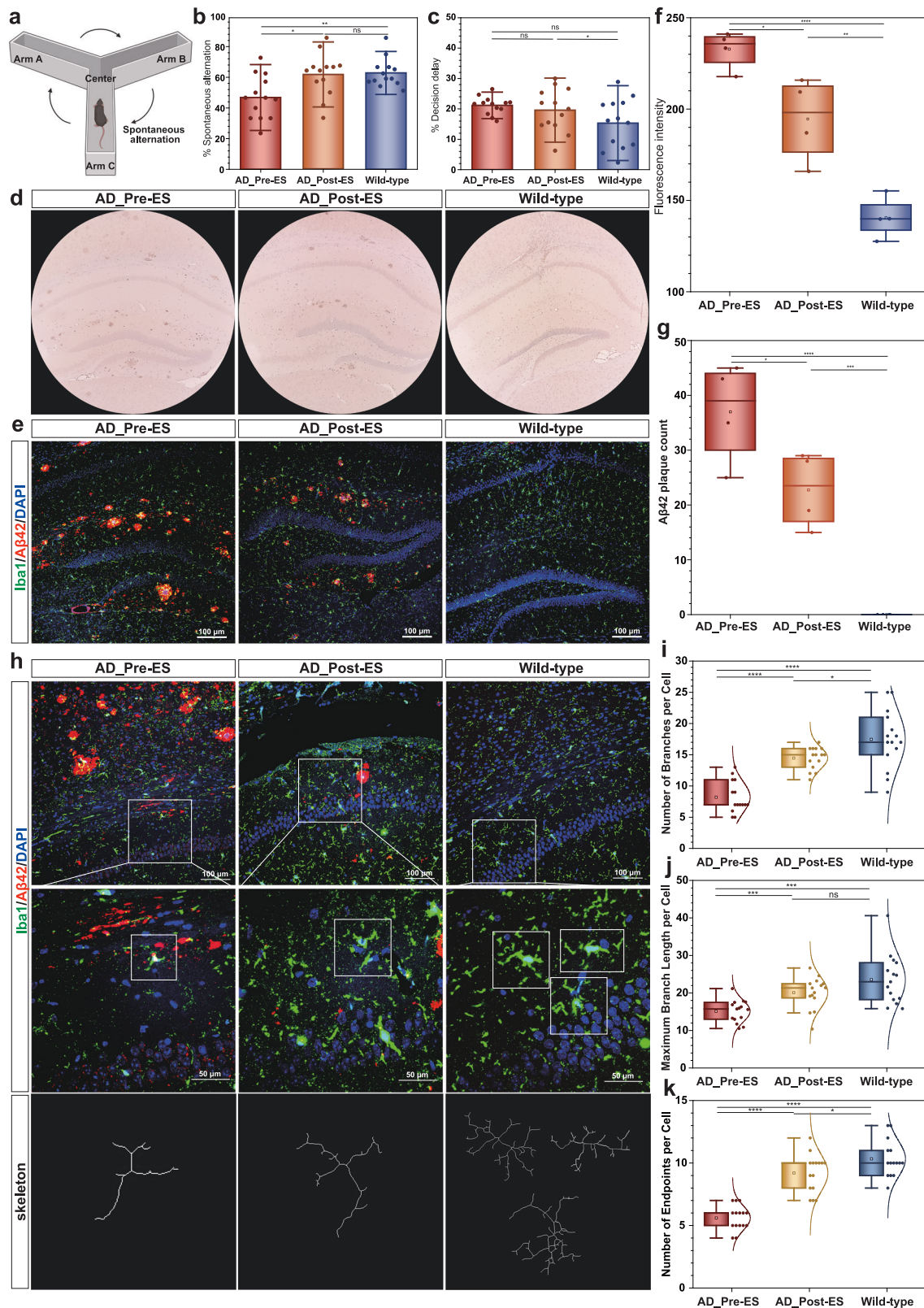
To more accurately assess the macrobehavioral changes in the mice, the decision delay in the center of the Y-maze was used as an indirect indicator of spatial decision-making behavior in mice. This was defined as the percentage of time spent making a decision relative to the total time. The decision delay of APP/PS1 mice before ES was 21%, which increased slightly to 20% after ES. Wild-type mice had a decision delay of 15% (Fig. 6c).

Additionally, immunohistochemistry and immunofluorescence staining were performed to evaluate the impact of 40 Hz ES on the neural molecules and cells of APP/PS1 mice. The results suggest that 40 Hz ES may influence molecular and cellular markers, including possible reductions in A β ₄₂ deposition and alterations in microglial morphology. A substantial reduction in A β ₄₂ deposition was observed in the DG and CA1 regions (Fig. 6d–g). The results of the negative control experiment for IHC are presented in Figure. S11. In healthy wild-type mice, microglia can phagocytose and clear waste, damaged cells, and a small amount of amyloid-beta (A β), helping to remove extracellular harmful substances and maintain neuronal health. However, in APP/PS1 mice, microglial cells exhibit reduced efficiency in clearing A β , leading to significant A β accumulation. This inefficiency may also exacerbate neurodegeneration through excessive release of inflammatory factors. Regarding microglial morphology, wild-type mice exhibited a greater number of branches, longer maximum branch length, and more branch endpoints, allowing them to sense and monitor the surrounding environment and perform routine neuroprotective functions (Fig. 6h–k). In AD mice, 40 Hz stimulation significantly increased the number of branches, maximum branch length, and branch endpoints, suggesting a potential shift in microglial status toward a more activated phenotype. In contrast, microglia in unstimulated APP/PS1 mice exhibited fewer branches, shorter maximum branch length, and a reduced number of branch endpoints (Fig. 6h–k). While ES appeared to modulate microglial morphology in APP/PS1 mice, the changes did not fully resemble those seen in wild-type mice, and the functional implications remain to be clarified.

Discussion

The abnormal deposition of A β and tau proteins promotes hippocampal long-term depression, which is considered a central mechanism leading to synaptic dysfunction in AD¹. Additionally, dysfunction in dopaminergic neurons also contributes to AD progression^{11,43,44}, impairing synaptic plasticity in the hippocampus and disrupting neuronal communication⁴⁵, which results in memory decline and impaired spatial cognition^{46,47}. The reduction in DA levels triggers neuroinflammation, potentially exacerbating A β accumulation and pathological development⁸. Therefore, the dysfunction of hippocampal dopaminergic neurons and the significant decrease in DA levels may offer crucial targets for early intervention and treatment^{10,48}.

Dopaminergic neurons associated with cognitive function are primarily concentrated in the ventral tegmental area (VTA) and locus coeruleus (LC), and the hippocampus receives dopaminergic projections from both VTA and LC^{49,50}. In the early stages of AD in mouse models, the accumulation of A β and tau in the hippocampus is relatively low, allowing dopaminergic neurons to retain partial receptor functionality⁴⁸. ES of the CA1 regions locally activates the axon terminals of dopaminergic neurons, causing depolarization and opening voltage-gated sodium and calcium channels, which in turn triggers the release of DA from synaptic vesicles. Additionally, ES of the CA1 regions enhances the excitability of glutamatergic neurons, promoting a balanced interaction between DA and glutamate⁵¹, further increasing DA release. Furthermore, this stimulation may activate neural networks connected to the hippocampus, exerting long-range modulation. The depolarization signal propagates to the dopaminergic



pathways within the mesolimbic system⁵⁰, inducing a shift in dopaminergic neurons in the VTA or LC from tonic firing to burst firing^{52,53}, thereby increasing DA release. This enhanced release is projected to the hippocampus via long axonal projections, a phenomenon observed in our electrophysiological recordings.

In current research, 40 Hz stimulation has been explored as a treatment for AD, including optogenetic modulation, multisensory

stimulation, and transcranial alternating current stimulation (tACS)⁵⁴. Animal studies have shown that 40 Hz optogenetic flicker stimulation reduces Aβ deposition in the hippocampus⁵⁵. Moreover, it alters the morphology and function of microglia, enhancing their ability to phagocytose Aβ plaques⁵⁵. Combined auditory and visual multisensory stimulation has also significantly decreased Aβ deposition in the hippocampus and improved memory^{56–59}. Clinical studies have validated

Fig. 6 | Behavioral, neuro-molecular, and cellular changes in APP/PS1 mice pre- and post-Electrical-Stimulation (ES). **a** Y-maze test paradigm. **b** Percentage of correct spontaneous alternation behavior in wild-type and APP/PS1 mice pre- and post-ES ($n = 13$ wild-type mice and $n = 13$ APP/PS1 mice; data are presented as mean \pm s.d.; P values: AD_Pre-ES vs. AD_Post-ES, $P = 0.0133$; AD_Pre-ES vs. wild-type, $P = 0.0025$; AD_Post-ES vs. wild-type, $P = 0.8161$). **c** Percentage of decision time spent at the center of the maze in wild-type and APP/PS1 mice pre- and post-ES ($n = 13$ wild-type mice and $n = 13$ APP/PS1 mice; data are presented as mean \pm s.d.; P values: AD_Pre-ES vs. AD_Post-ES, $P = 0.4568$; AD_Pre-ES vs. wild-type, $P = 0.0231$; AD_Post-ES vs. wild-type, $P = 0.1675$). **d** $A\beta_{42}$, and nuclear immunohistochemistry staining in the hippocampus of wild-type and APP/PS1 mice pre- and post-stimulation ($A\beta_{42}$: brown, Hematoxylin: blue). **e** Microglia, $A\beta_{42}$, and nuclear immunofluorescence staining in the hippocampus of wild-type and APP/PS1 mice pre- and post-stimulation ($Iba1$: green, $A\beta_{42}$: red, DAPI: blue). **f** Immunofluorescence intensity in the hippocampus of wild-type and APP/PS1 mice pre- and post-stimulation (P values: AD_Pre-ES vs. AD_Post-ES, $P = 0.0225$; AD_Pre-ES vs. wild-type, $P = 0.0054$; AD_Post-ES vs. wild-type, $P < 0.0001$). **g** $A\beta_{42}$ plaque count in the hippocampus of wild-type and APP/PS1 mice pre- and post-stimulation (P values: AD_Pre-ES vs. AD_Post-ES, $P = 0.0463$; AD_Pre-ES vs. wild-type, $P = 0.0006$; AD_Post-

ES vs. wild-type, $P = 0.0002$). (**f**, **g**: $n = 4$ independent samples for all data; data are presented as mean \pm s.d.; Box plots show the median as a center line, the interquartile range as the box, minimum to maximum values as whiskers, individual samples as dots, and group means as white squares.). **h** Immunofluorescence staining of microglia, $A\beta_{42}$, and nuclei in the hippocampal CA1 region of wild-type and APP/PS1 mice before and after stimulation ($Iba1$: green, $A\beta_{42}$: red, DAPI: blue), along with the astrocytic cytoskeleton. **i–k** Quantification of astrocyte morphology in wild-type and APP/PS1 mice before and after stimulation: **i** Number of branches per single cell (P values: AD_Pre-ES vs. AD_Post-ES, $P < 0.0001$; AD_Pre-ES vs. wild-type, $P < 0.0001$; AD_Post-ES vs. wild-type, $P = 0.0267$). **j** Maximum branch length per cell (P values: AD_Pre-ES vs. AD_Post-ES, $P = 0.0008$; AD_Pre-ES vs. wild-type, $P = 0.0001$; AD_Post-ES vs. wild-type, $P = 0.0998$). **k** Number of branch endpoints per single cell (P values: AD_Pre-ES vs. AD_Post-ES, $P < 0.0001$; AD_Pre-ES vs. wild-type, $P = 0.0485$; AD_Post-ES vs. wild-type, $P < 0.0001$). (**i–k**: $n = 15$ independent samples for all data; data are presented as mean \pm s.d.; Box plots show the median as a center line, the interquartile range as the box, minimum to maximum values as whiskers, individual samples as dots, and group means as white squares.). Statistical significance was assessed by unpaired two-tailed Student's t -tests. ns, not significant ($p \geq 0.05$); * $p < 0.05$, ** $p < 0.01$, *** $p < 0.001$, **** $p < 0.0001$.

that 40 Hz visual/auditory stimulation slows brain atrophy in AD patients^{60,61} and improves sleep quality⁶². The cognitive-enhancing effects of 40 Hz tACS have been confirmed, particularly in logical reasoning⁶³ and language insight⁶⁴. It is currently hypothesized that gamma frequencies are closely associated with higher-order cognitive activities, with 40 Hz stimulation inducing neural group resonance, thereby enhancing cognitive functions. Together, these studies highlight the potential of 40 Hz stimulation in AD treatment, providing strong scientific support for its selection as a preferred frequency for brain stimulation.

Optogenetic stimulation relies on genetic manipulation and viral transfection, which pose ethical and safety challenges in human experiments⁶⁵. Additionally, light penetration in tissue is limited (< 1 cm)⁶⁶, making it difficult to effectively target deep brain regions. In contrast, FlexChip ES offers stable stimulation frequencies with precise targeting of brain regions, minimizing interference from undesired frequency bands. Moreover, electrophysiological recordings of neural populations and single neurons demands high precision and resolution. Similarly, the electrochemical responses are subtle (at the nA and μ A levels)⁶⁷. Neurotransmitter fluctuations are restored quickly, and the signal differences from baseline are often minimal, making them difficult to capture. This is a key limitation that prevents further advancement of extracranial devices like tACS. FlexChip not only integrates electrophysiological recording, DA detection, and ES control, but also provides real-time, multidimensional feedback. It operates efficiently while minimizing tissue damage, making it a superior tool for research and therapeutic applications.

Neuronal hyper-synchronization firings have been observed in both AD patients and animal models, with some pathological features overlapping with those seen in epilepsy patients^{34,35}. Hyper-synchronization firings may be related to dopaminergic dysfunction, including changes in the expression of specific DA receptors⁶⁸ and increased firing of DA neurons. Activation of D1-like receptors (e.g., D1 and D5) promotes neuronal excitability, while activation of D2-like receptors (e.g., D2, D3, D4) inhibits neuronal activity⁶⁹. Therefore, activation of D1 receptors lowers the seizure threshold and increases the risk of seizures, while antagonizing D2 receptors can suppress neuronal excitability. Currently, DBS is recognized as a treatment for epilepsy, modulating the dopaminergic system to influence seizure-related neuronal discharges. Additionally, imbalances in other neurotransmitters may also trigger epileptiform discharges, particularly dysfunction in glutamatergic and GABAergic neurons, as well as acetylcholine and 5-HT systems.

In the future, FlexChip stimulation therapy could be applied not only to research on the stimulation mechanisms and treatment of

AD, but also extended to other neurological disorders associated with neurotransmitter imbalances. Of course, there is still room for development in comprehensive neurotransmitter detection and multi-brain-region analysis. In terms of comprehensive neurotransmitter detection, it would be beneficial to add the capability to detect glutamate, GABA, and 5-HT. By analyzing multiple neurotransmitters synergistically, we can explore the complex interactions between AD and various neurotransmitters more deeply. For multi-brain-region detection, given the wide projection range of neurotransmitters, adding more electrodes or using single-shank multi-electrode implants to simultaneously test both upstream and downstream regions of neurotransmitter projections (e.g., cortex and VTA) would significantly advance the application of electrochemical regulation in the treatment of neurodegenerative diseases.

Methods

Animals

All animal care and procedures adhered to the guidelines set by the Institutional Animal Care and Use Committee at the Aerospace Information Research Institute, Chinese Academy of Science (AIRCAS), and were approved by the Beijing Laboratory Animal Care Association and the AIRCAS Animal Care and Use Committee under approval number AIRCAS-202103-1.

Thirty male mice were used: wild-type mice (C57BL/6 N) ($n = 15$) supplied by Charles River Laboratory Animal Technology Co., Ltd., Beijing, China, and APP/PS1 AD mice ($n = 15$) supplied by Zhishan Institute of Health Medicine Co., Ltd., Beijing, China. At the time of the neurophysiological and electrochemical signal tests, the mice were six months old and had body weights of 25.4 ± 0.2 g and 25.8 ± 0.1 g, respectively (mean \pm SEM). The mice were maintained at 20 °C and 40–60% relative humidity under a 12-hour light/dark cycle. The experimental APP/PS1 mouse is a widely used AD model. APP/PS1 mice are generated through transgenic techniques by introducing the Swedish mutant amyloid precursor protein gene (*APP695swe*) and the human presenilin 1 gene with exon 9 deletion (*PSEN1 Δ E9*) into the mouse genome. Under the control of a tissue-specific promoter, these two genes are highly expressed in the central nervous system of the mice, leading to significant accumulation of $A\beta$ amyloid in the brain tissue. As the mice age, the brain develops amyloid plaques formed by the aggregation of β -amyloid protein, accompanied by cognitive and behavioral decline as well as other AD-related pathological changes. In the brains of APP/PS1 mice, neuronal degeneration and synaptic damage can be observed, including a reduction in synaptic density and neuronal loss.

Fabrication of the NeuroRevive-FlexChip

The NeuroRevive-FlexChip fabrication relies on Micro-Electro-Mechanical System technology and requires four layers of masks for pattern definition. The specific steps of the fabrication process are as follows:

Parylene deposition. On a clean silicon wafer, a 6 μm parylene layer is deposited using Chemical Vapor Deposition (CVD), serving as the bottom flexible carrier layer for the NeuroRevive-FlexChip (Fig. 1d (i)).

First photolithography. Photoresist AZ5214 is spin-coated onto the parylene surface, defining the pattern for the deep conductive layer (Fig. 1d (ii–iii)).

Deep conductive layer formation. The Cr/Au (30/200 nm) is sputtered through physical vapor deposition (PVD) and lifted off to form the deep conductive layer (Fig. 1d (iv–v)).

Isolation layer. A 2 μm parylene layer is deposited using CVD to isolate the deep conductive layer from the shallow conductive layer (Fig. 1d (vi)).

Second photolithography. Photoresist AZ5214 is spin-coated onto the parylene surface, defining the pattern for the shallow conductive layer (Fig. 1d (vii)), repeating step (2).

Shallow conductive layer formation. The Cr/Au (30/200 nm) is sputtered through PVD and lifted off to form the shallow conductive layer (Fig. 1d (viii)), repeating step (3).

Top isolation layer. A 2 μm parylene layer is deposited using CVD to form the top flexible insulation layer for the NeuroRevive-FlexChip (Fig. 1d (ix)), repeating step (4).

Third photolithography. AZ4620 is spin-coated onto the top parylene layer, defining sites for etching and the overall outline of the NeuroRevive-FlexChip (Fig. 1d (x–xi)).

Plasma etching. Oxygen plasma etching exposes detection, stimulation, counter, reference micro-electrodes, bonding pads, and the overall outline of the NeuroRevive-FlexChip (Fig. 1d (xii)).

Fourth photolithography. AZ4903 is spin-coated onto the top parylene layer, defining only the overall outline of the NeuroRevive-FlexChip (Fig. 1d (xiii–xiv)).

Final plasma etching. Oxygen plasma etching defines the overall outline of the NeuroRevive-FlexChip. After cleaning, the NeuroRevive-FlexChip is obtained (Fig. 1d (xv)).

Surface modification of the neurorevive-FlexChip

The NeuroRevive-FlexChip incorporates functional micro-electrodes for electrophysiology, electrochemistry detection, and ES. Optimal performance of detection microelectrodes requires low impedance and minimal phase delay at 1 kHz. Moreover, the electrochemical detection micro-electrodes need to exhibit low oxidation-reduction potential, high sensitivity, and selectivity for DA detection. Consequently, PtNPs/PEDOT:PSS/MWCNTs (xfnano) modification was employed for both types of microelectrodes. Subsequently, a thin Nafion ion exchange membrane layer was delicately coated on the microelectrode surface. To optimize the charge storage capacity of the stimulation microelectrodes on the NeuroRevive-FlexChip, three modification schemes were electroplated and evaluated at micro-electrodes with a diameter of 20 μm . The modification schemes are

PtNPs/PPy/MWCNTs, PtNPs/PEDOT:PSS/MWCNT, and PtNPs/PEDOT:PSS/PPy/MWCNTs.

PtNPs are pivotal in enhancing micro-electrode roughness, substantially reducing microelectrode impedance, minimizing phase delay, and facilitating the attachment of PEDOT:PSS or PPy. Therefore, all micro-electrodes were initially modified with PtNPs. The PtNPs solution involves mixing 48 mM H_2PtCl_6 and 4.2 mM $\text{Pb}(\text{CH}_3\text{COO})_2$ in a 1:1 ratio, which was then electrodeposited using a two-electrode system through the chronoamperometry (IT) method with a potential of -1.2 V for 60 s.

Following this, different modifications were applied to individual micro-electrodes.

For the PPy/MWCNTs composite modification, 8 mg of MWCNTs (xfnano) was dissolved in 20 ml ddH_2O , sonicated for 30 minutes, and then combined with 2 mM PPy (sigma). Further sonication was employed until homogeneity was achieved. Electrodeposition was conducted using CV in the potential range of 0–0.3 V at a scan rate of 100 mV/s for 1 cycle.

In the case of the PEDOT:PSS/MWCNTs composite modification, 8 mg of MWCNTs were dissolved in 20 ml ddH_2O , sonicated for 30 minutes, and combined with 0.2 M PSS (Alfa Aesar). After an additional 30 minutes of sonication, 40 mM EDOT (Clevios) was added, and further sonication ensued until complete homogeneity was attained. Electrodeposition is performed using CV in the potential range of 0–0.95 V at a scan rate of 100 mV/s for 5 cycles.

Subsequently, the microelectrode was electrodeposited with the PPy/MWCNTs colloid using CV in the potential range of 0–0.3 V at a scan rate of 100 mV/s for 1 cycle.

Finally, a Nafion (Shanghai Aladdin Biochemical Technology Co., Ltd) coating was executed: using a pipette, 10 μL of Nafion was repeatedly dropped onto the electrode sites three times. Subsequently, the electrode was baked under a lamp for 20 minutes, and after 12 hours of Nafion film stabilization, it was ready for use.

The performance characterization of the NeuroRevive-FlexChip

The NeuroRevive-FlexChips are evaluated by capturing SEM images of microelectrodes with different materials, testing electrical performance, assessing DA (MACKLIN) response, and measuring charge storage capacity in electrophysiological, electrochemical, and ES microelectrodes.

SEM images were captured for microelectrodes modified with PtNPs/PPy/MWCNTs, PtNPs/PEDOT:PSS/MWCNTs, and PtNPs/PEDOT:PSS/PPy/MWCNTs. Electrical performance was assessed through electrochemical impedance spectroscopy (EIS), measuring impedance and phase delay. The electrochemical performance involved CV scanning ($-0.3 - 0.6\text{ V}$) microelectrodes in PBS and a 200 μM DA solution to determine DA oxidation reaction potential. The response curve to DA was measured using chronoamperometry. Charge storage capacity testing utilized CV scanning (-1.5 to 1.5 V) to determine the water window (Figure. S5). In the water window range, CV scanning (-0.6 to 0.6 V) determined the modified materials' double-layer capacitance and charge storage capacity.

After modification with different materials, the surface area of the microelectrode changes with varying roughness. Here, correction is applied to the microelectrodes' surface area⁷⁰:

$$A_{\text{Bare}}/A_{\text{real}} = R_{\text{real}}/R_{\text{Bare}}A_{\text{real}} = (R_{\text{Bare}}/R_{\text{real}})A_{\text{Bare}} \quad (1)$$

where A_{bare} and R_{bare} represent the geometric surface area of the bare microelectrode and the impedance in PBS solution, respectively. A_{real} and R_{real} denote the surface area of the modified microelectrode and the impedance in the PBS solution, respectively.

The double-layer capacitance is calculated by taking the current difference Δj at a specific voltage in a 100 mV/s scan rate from the CV

curve, then dividing it by the scan rate v and the surface area A of the detection microelectrode⁷¹.

$$C_{dl} = \frac{\Delta_j}{vA} \quad (2)$$

The charge storage capacity can be calculated by integrating the area under the CV curve and dividing it by the scan rate v and the surface area A of the detection microelectrode⁷².

$$CSC = \oint \frac{i}{vA} dE \quad (3)$$

The stimulation electric field simulation of the NeuroRevive-FlexChip

We conducted an ES simulation using COMSOL Multiphysics, focusing on the NeuroRevive-FlexChip implanted in a mouse brain. In our model, the mouse brain is simulated as a cerebrospinal fluid environment with an electrical conductivity of 2 S/m and a relative permittivity of 109. The stimulation utilizes platinum material for its high conductivity of 8.9×10^6 S/m and a relative permittivity of 1. The NeuroRevive-FlexChip carrier is made of parylene, characterized by an extremely low conductivity of 10^{-20} S/m and a relative permittivity of 10. In our simulation setup, the concentric outer ring of the stimulation carries a current of 300 μ A, while the skull surface and the concentric inner ring of the stimulation are grounded, replicating actual field and grounding conditions. Additionally, the NeuroRevive-FlexChip carrier and other brain surfaces are set as electrically insulating. This setup allows us to simulate the distribution of the NeuroRevive-FlexChip's stimulation electric field within the mouse brain and assess its impact on the targeted detection microelectrodes.

The NeuroRevive-FlexChip electrochemical response in vitro stimulation

The electrochemical workstation is used to monitor the electrochemical response of the NeuroRevive-FlexChip. Initially, the detection microelectrodes of the NeuroRevive-FlexChip are immersed in an extracellular PBS solution with a silver/silver chloride (Ag/AgCl) reference electrode and a platinum (Pt) counter electrode. The working electrode is connected to the electrochemical detection microelectrodes. The stimulation microelectrode is linked to a custom-made stimulation device (AIRCAS-128, China)⁷³, providing the same parameters as in vivo stimulation: 40 Hz frequency, 0.06 s pulse width, and bidirectional current stimulation of 100 μ A, 200 μ A, and 300 μ A for 200 s each. It was observed that the current detected by the electrochemical workstation remained relatively constant during the stimulation process (Fig. 1e).

Animal surgery procedure

Animal surgery has three main parts: preoperative preparation, animal surgery, and postoperative brain retrieval.

Firstly, PEG2000 (MACKLIN) is melted in a water bath at 70 °C for preoperative preparation until entirely transparent. A small amount is then taken with a 10 ml syringe needle and thinly coated on the surface of the NeuroRevive-FlexChip. After a few minutes, wait until the PEG hardens and turns white. Subsequently, the NeuroRevive-FlexChip is inserted into a 0.6% agar solution and withdrawn after 3 s, causing the surface PEG portion to dissolve. This ensures a small amount of thin PEG remains on the implant shaft of the NeuroRevive-FlexChip, serving a reinforcing purpose while minimizing electrode thickening.

Next, the animal surgery begins. The operating table and all surgical instruments are cleaned and disinfected with ultraviolet light or alcohol. The mouse is anesthetized with 5% isoflurane until the heart rate is 1 beat/s. The anesthesia concentration is adjusted to 1.5%, and

the mouse is fixed on a stereotaxic instrument. The anesthesia maintenance concentration is 0.9% (RWD520, Shenzhen RWD LifeScience Co., Ltd., Shenzhen, China). The mouse's fur and scalp are successively removed. A small window of 1.5 mm \times 1.5 mm is opened in the right hemisphere of the mouse, and the meninges are removed. The NeuroRevive-FlexChip is implanted in the hippocampal CA1 region pathway (AP: 2.3, ML: +2, DV: 1.4 to 1.6 relative to bregma)⁷⁴. The mouse's skull is kept dry throughout the surgery while maintaining the brain tissue moist. After the electrode implantation is complete, excess PEG on the surface of the electrode is melted with a gelatin sponge soaked in physiological saline. Dental cement is applied around the electrode to ensure relative fixation between the electrode and brain tissue.

Finally, after completing signal detection, the mouse undergoes cardiac perfusion with physiological saline and 4% paraformaldehyde for postoperative brain retrieval. The mouse's brain is removed and sequentially immersed in 20% and 30% sucrose solutions until sinking. Finally, the brain is frozen and sliced to observe the implantation location of the electrode (Figure. S6).

Experimental platform

The experimental platform includes an electromagnetic shielding cage, an integrated electrophysiological recording and ES system (AIRCAS-128, China), and an electrochemical workstation (Gamry Reference 600, Gamry Instruments, USA) (Fig. 7a). Three days after surgery, the mouse's head was securely positioned inside the electromagnetic shielding cage, with the FlexChip connected to the neural signal processing headstage. The setup was then connected via wires to the integrated electrophysiological recording and ES system and the electrochemical workstation.

40 Hz ES protocol

Prolonged and continuous ES can result in neural activity tolerance⁷⁵ and may even cause uncontrollable neural firings⁷⁶. Therefore, a discrete stimulation protocol was implemented: six 400 s current pulses, each separated by a rest period of at least 5 minutes, cumulatively exceeding 30 minutes (Fig. 7b). Mice rested for a minimum of 5 minutes between each stimulation session. Electrical currents were varied, set to 100 μ A for 1 session, 200 μ A for 2 sessions, and 300 μ A for the remaining 3 sessions. Stimulate at a fixed time period every evening with a current of 300 μ A for seven consecutive days. At the start of each stimulation, the mice briefly move slightly and then return to a resting state. Electrophysiological recordings were initiated 2 minutes post-stimulation to minimize stimulation artifacts.

Electrophysiological, electrochemical recording and analysis

Mice are acclimated in the shielding cage for at least 30 minutes, and the electrochemical current response curves are monitored until they stabilize. After the electrochemical baseline is stable, electrochemical DA current response signals are recorded, and the electrochemical recording continues throughout the experiment without interruption. Next, the electrophysiological signals are recorded for 5 min before stimulation. Subsequently, the first 100 μ A, 40 Hz ES is initiated, lasting for 400 s. Due to the noise introduced by ES causing distortion of electrophysiological signals, electrophysiological signals are not recorded during the stimulation process. After the stimulation ends, a 200–300 s wait is required to ensure no stimulation artifacts are present before recording the electrophysiological signals for 5 min. Following this, the paradigm is repeated with 2 sessions of 200 μ A and 3 sessions of 300 μ A ES and electrophysiological signal recording.

The laboratory's self-made integrated electrophysiological recording and ES system performs multi-stage filtering and amplification of the electrophysiological signals captured by the FlexChip. The electrophysiological signal sampling rate is set at 30 kHz, with a high-pass filter at a cutoff frequency of 250 Hz to obtain spikes and a

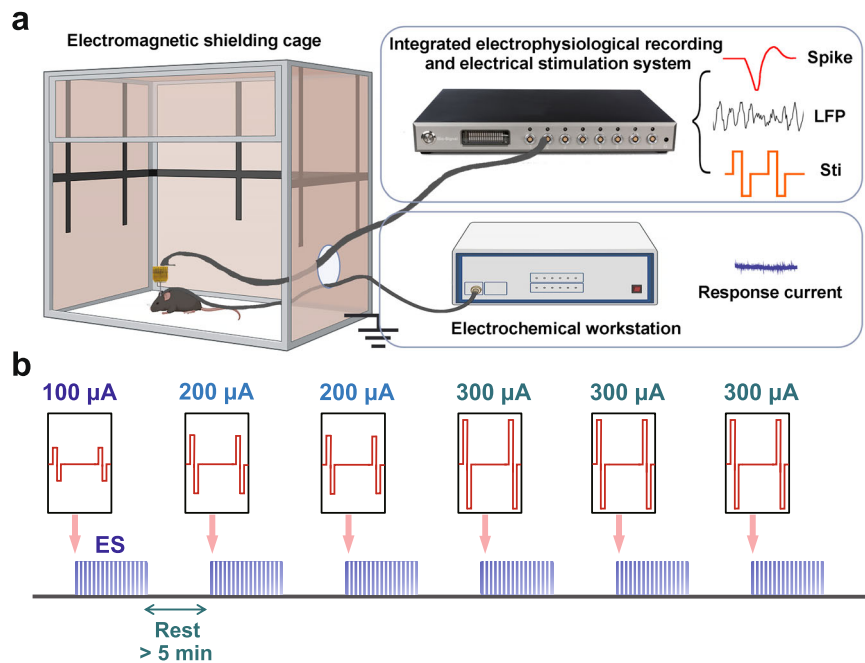


Fig. 7 | Experimental setup and electrical stimulation (ES) protocol design. **a** Experimental setup (including a shielded cage, integrated electrophysiological recording and ES system, and electrochemical workstation). **b** 40 Hz discrete ES

protocol (six 400 s current pulses: one pulse at 100 μA , two pulses at 200 μA , and three pulses at 300 μA , with at least 5 min of rest between stimulations). a Created in BioRender. Lv, S. (2025) <https://BioRender.com/0sxum4f>.

low-pass filter at a cutoff frequency of 250 Hz to obtain LFPs. The electrochemical signals are recorded by the electrochemical workstation (Gamry Reference 600, Gamry Instruments, USA).

Spike sorting/clustering was performed using Offline Sorter. Neuronal signals were classified based on waveform parameters such as spike amplitude and principal components. Clusters containing similar valid waveforms were manually sorted to ensure that the refractory period of single units was no less than 1 ms. Finally, the recorded electrophysiological signals were aligned with the electrochemical signals on the time axis.

Behavioral testing, recording, and analysis

The Y-maze consists of three equal-length arms, each 28 cm long, 5 cm wide, and with walls 10 cm high. The angle between the arms is 120°. The experiment includes three groups of mice: wild-type mice implanted with electrodes, APP/PS1 mice implanted with electrodes but not receiving ES, and APP/PS1 mice implanted with electrodes that received ES. To avoid odor cues, the maze surface was wiped with 70% ethanol and then rinsed with water after each trial. At the start of each trial, the mouse was placed in the central connecting area of the maze and allowed to explore freely. When the mouse entered more than 25% of an arm's length, it was considered to have entered that arm for exploration. Depending on the mouse's activity, the experiment duration was recorded for 5 to 10 minutes. During the experiment, an optical camera was positioned above the Y-maze to track the mouse's movement. Behavioral analysis software (EthoVision XT 15, Noldus, China) recorded the XY coordinates of the mouse's movement and measured the number of correct spontaneous alternations, total possible alternations, and the time spent in both the arms and the central area. A correct spontaneous alternation was defined as the mouse consecutively entering three different arms (e.g., entering Arm A, B, and C in sequence would count as one correct alternation). The total possible alternations were calculated as the total number of arm entries minus 2. Additionally, the time spent in the central area of the Y-maze was defined as decision-making delay before entering an arm.

Based on the data above, the spontaneous alternation accuracy and decision delay percentage of the mice are calculated as follows:

$$\text{Spontaneous alternation accuracy} = \frac{\text{correct alternations}}{\text{Total possible alternations}} \times 100\%$$

$$\text{Decision delay percentage} = \frac{\text{Time spent in center area}}{\text{Total time spent in the Y maze}} \times 100\%$$

Immunohistochemistry and immunofluorescence staining

Perfusion and paraffin sectioning. Perfusion and tissue processing were performed on wild-type mice, APP/PS1 mice implanted with electrodes without stimulation, and APP/PS1 mice implanted with electrodes and stimulated at 40 Hz. After anesthetizing the mice, they were perfused with saline in a volume equal to their body weight, followed by 4% paraformaldehyde in a volume equal to their body weight. The brains were extracted, immersed in 4% paraformaldehyde, and fixed by refrigeration for at least one day. Following fixation, the tissues were paraffin-embedded and sectioned at a thickness of 5 μm in the coronal plane. Sections were deparaffinized and subjected to antigen retrieval. The sections were divided into two groups, one for immunohistochemistry and the other for immunofluorescence staining.

Immunohistochemistry (IHC). To reduce nonspecific staining, 3% H_2O_2 was applied to the sections and incubated in the dark for 25 minutes, followed by washing. Sections were then blocked with 3% BSA for 25 minutes, and primary antibodies anti-A β 42 (1:50 dilution, rabbit monoclonal [mOC98], Abcam, catalog #ab201061, lot [1028231-16]) and Iba1 (0.1 $\mu\text{g}/\text{ml}$, rabbit monoclonal antibody [EPRI6588], Abcam, catalog #ab178846, lot [1090399-9]) were added, incubating overnight at 4 °C. After three washes in 0.1M PBS at room temperature, sections were incubated with secondary antibody (#511203, ZENBIOSCIENCE). DAB substrate was added to visualize positive staining in

brown. After DAB development, the reaction was stopped by rinsing with tap water, and the nuclei were counterstained with hematoxylin.

Immunofluorescence Staining. To reduce nonspecific background staining, 3% H₂O₂ was applied and incubated in the dark for 30 minutes, followed by washing. Sections were permeabilized in 0.1% Triton-100X for 30 minutes at room temperature, and then blocked with 3% BSA for 30 minutes to prevent nonspecific protein binding. Primary antibodies anti-A β ₄₂ (1:50, #ab201061, Abcam) and Iba1 (0.1 μ g/ml, #ab178846, Abcam) were added and incubated overnight at 4 °C. After three washes in 0.1M PBS at room temperature, diluted secondary antibodies (#550037, #550043, ZEN-BIOSCIENCE) were applied for incubation. DAPI was used for nuclear counterstaining, and sections were mounted with an anti-fade mounting medium. Imaging was performed using a laser scanning confocal microscope (LSM900, Zeiss) to capture the images.

Statistical analysis

All quantitative results are presented as mean \pm SE, with the displayed percentages representing the group mean. Electrophysiological signals were analyzed using Offline Sorter for spike sorting and clustering. Neurons were classified based on waveform parameters such as spike amplitude and principal components. Neuronal clusters with similar valid waveforms were manually defined, ensuring that the refractory period for individual units was no less than 1 ms. All fluorescence intensity analysis, A β quantification, and astrocyte and microglial morphology analysis were performed using Image J software (National Institutes of Health, Bethesda, MD, USA). All statistical analyses were performed using Microcal Origin Pro 8.5.1 (OriginLab Corp., Northampton, MA, USA) and GraphPad Prism 9 software (GraphPad Software Inc., San Diego, USA). Statistical significance was assessed using a two-tailed t-test, with a *p*-value < 0.05 considered statistically significant. Significance levels were denoted as follows: **P* < 0.05, ***P* < 0.01, ****P* < 0.001, *****P* < 0.0001.

Reporting summary

Further information on research design is available in the Nature Portfolio Reporting Summary linked to this article.

Data availability

All data supporting the findings of this study are available within the article and its supplementary files. Any additional requests for information can be directed to, and will be fulfilled by, the corresponding authors. Source data are provided with this paper.

References

- O'Riordan, K. J., Hu, N.-W. & Rowan, M. J. A β facilitates LTD at Schaffer collateral synapses preferentially in the left hippocampus. *Cell Rep.* **22**, 2053–2065 (2018).
- Braak, H. & Braak, E. Neuropathological staging of Alzheimer-related changes. *Acta Neuropathol.* **82**, 239–259 (1991).
- Moreno-Jiménez, E. P. et al. Adult hippocampal neurogenesis is abundant in neurologically healthy subjects and drops sharply in patients with Alzheimer's disease. *Nat. Med.* **25**, 554–560 (2019).
- Knopman, D. S. et al. Alzheimer disease. *Nat. Rev. Dis. Prim.* **7**, 33 (2021).
- Hardy, J. & Allsop, D. Amyloid deposition as the central event in the aetiology of Alzheimer's disease. *Trends Pharm. Sci.* **12**, 383–388 (1991).
- Augustinack, J. C., Schneider, A., Mandelkow, E.-M. & Hyman, B. T. Specific tau phosphorylation sites correlate with severity of neuronal cytopathology in Alzheimer's disease. *Acta Neuropathol.* **103**, 26–35 (2002).
- Gazestani, V. et al. Early Alzheimer's disease pathology in human cortex involves transient cell states. *Cell* **186**, 4438–4453.e23 (2023).
- Tzioras, M., McGeachan, R. I., Durrant, C. S. & Spires-Jones, T. L. Synaptic degeneration in Alzheimer's disease. *Nat. Rev. Neurol.* **19**, 19–38 (2023).
- Leng, F. et al. Neuroinflammation is independently associated with brain network dysfunction in Alzheimer's disease. *Mol. Psychiatry* **28**, 1303–1311 (2023).
- Pan, X. et al. Dopamine and dopamine receptors in Alzheimer's disease: a systematic review and network meta-analysis. *Front. Aging Neurosci.* **11**, 175 (2019).
- Nobili, A. et al. Dopamine neuronal loss contributes to memory and reward dysfunction in a model of Alzheimer's disease. *Nat. Commun.* **8**, 14727 (2017).
- Koch, G. et al. Effect of Rotigotine vs Placebo on cognitive functions among patients with mild to moderate Alzheimer disease: a randomized clinical trial. *JAMA Netw. Open* **3**, e2010372 (2020).
- Andres, E. et al. Replication study on the role of dopamine-dependent prefrontal reactivations in human extinction memory retrieval. *Nat. Commun.* **15**, 2699 (2024).
- Motiwala, A., Soares, S., Atallah, B. V., Paton, J. J. & Machens, C. K. Efficient coding of cognitive variables underlies dopamine response and choice behavior. *Nat. Neurosci.* **25**, 738–748 (2022).
- Barnby, J. M., Bell, V., Deeley, Q., Mehta, M. A. & Moutoussis, M. D2/D3 dopamine supports the precision of mental state inferences and self-relevance of joint social outcomes. *Nat. Ment. Health* **2**, 562–573 (2024).
- Shoob, S. et al. Deep brain stimulation of thalamic nucleus reuniens promotes neuronal and cognitive resilience in an Alzheimer's disease mouse model. *Nat. Commun.* **14**, 7002 (2023).
- Luo, Y. et al. Deep brain stimulation of the entorhinal cortex modulates CA1 theta-gamma oscillations in mouse models of preclinical Alzheimer's disease. *Biocybern. Biomed. Eng.* **43**, 246–260 (2023).
- McKinnon, C. et al. Deep brain stimulation: potential for neuroprotection. *Ann. Clin. Transl. Neurol.* **6**, 174–185 (2019).
- Suthana, N. et al. Memory enhancement and deep-brain stimulation of the entorhinal area. *N. Engl. J. Med.* **366**, 502–510 (2012).
- Violante, I. R. et al. Non-invasive temporal interference electrical stimulation of the human hippocampus. *Nat. Neurosci.* **26**, 1994–2004 (2023).
- Altomare, D. et al. Home-based transcranial alternating current stimulation (tACS) in Alzheimer's disease: rationale and study design. *Alz. Res. Ther.* **15**, 155 (2023).
- D'Amelio, M. & Di Lazzaro, V. Can transcranial magnetic stimulation rescue dopaminergic signalling in Alzheimer's disease?. *Brain* **146**, e43–e45 (2023).
- Jin, K. et al. Increased hippocampal neurogenesis in Alzheimer's disease. *PNAS* **101**, 343–347 (2004).
- Benussi, A. et al. Increasing brain gamma activity improves episodic memory and restores cholinergic dysfunction in Alzheimer's disease. *Ann. Neurol.* **92**, 322–334 (2022).
- Castagnola, E. et al. Stable in-vivo electrochemical sensing of tonic serotonin levels using PEDOT/CNT-coated glassy carbon flexible microelectrode arrays. *Biosens. Bioelectron.* **230**, 115242 (2023).
- Mo, F. et al. Single-neuron detection of place cells remapping in short-term memory using motion microelectrode arrays. *Biosens. Bioelectron.* **217**, 114726 (2022).
- Xu, Z. et al. Grid cell remapping under three-dimensional object and social landmarks detected by implantable microelectrode arrays for the medial entorhinal cortex. *Microsyst. Nanoeng.* **8**, 104 (2022).
- Mo, F. et al. Integrated three-electrode dual-mode detection chip for place cell analysis: dopamine facilitates the role of place cells in

- encoding spatial locations of novel environments and rewards. *ACS Sens* **12**, 4765–4773 (2023).
29. Tyler, W. J. The mechanobiology of brain function. *Nat. Rev. Neurosci.* **13**, 867–878 (2012).
30. Tang, X., Shen, H., Zhao, S., Li, N. & Liu, J. Flexible brain–computer interfaces. *Nat. Electron* **6**, 109–118 (2023).
31. Zhou, Z. D., Yi, L. X., Wang, D. Q., Lim, T. M. & Tan, E. K. Role of dopamine in the pathophysiology of Parkinson’s disease. *Transl. Neurodegener.* **12**, 44 (2023).
32. Monzani, E. et al. Dopamine, oxidative stress and protein–quinone modifications in parkinson’s and other neurodegenerative diseases. *Angew. Chem. Int. Ed.* **58**, 6512–6527 (2019).
33. Lohani, S. et al. Burst activation of dopamine neurons produces prolonged post-burst availability of actively released dopamine. *Neuropsychopharmacol* **43**, 2083–2092 (2018).
34. Palop, J. J. et al. Aberrant excitatory neuronal activity and compensatory remodeling of inhibitory hippocampal circuits in mouse models of alzheimer’s disease. *Neuron* **55**, 697–711 (2007).
35. Vossel, K. A., Tartaglia, M. C., Nygaard, H. B., Zeman, A. Z. & Miller, B. L. Epileptic activity in Alzheimer’s disease: causes and clinical relevance. *Lancet Neurol.* **16**, 311–322 (2017).
36. Westmark, C. J., Westmark, P. R., Beard, A. M., Hildebrandt, S. M. & Malter, J. S. Seizure susceptibility and mortality in mice that over-express amyloid precursor protein. *Int. J. Clin. Exp. Pathol.* **1**, 157–168 (2008).
37. Liu, Y. et al. Amyloid pathology is associated with progressive monoaminergic neurodegeneration in a transgenic mouse model of alzheimer’s disease. *J. Neurosci.* **28**, 13805–13814 (2008).
38. Storga, D., Vrecco, K., Birkmayer, J. G. D. & Reibnegger, G. Monoaminergic neurotransmitters, their precursors and metabolites in brains of Alzheimer patients. *Neurosci. Lett.* **203**, 29–32 (1996).
39. Cavaleiro, E. A., Fernandes, M. J., Turski, L. & Naffah-Mazzacoratti, M. G. Spontaneous recurrent seizures in rats: amino acid and monoamine determination in the hippocampus. *Epilepsia* **35**, 1–11 (1994).
40. Yang, J. et al. Dopaminergic modulation of axonal potassium channels and action potential waveform in pyramidal neurons of prefrontal cortex. *J. Physiol.* **591**, 3233–3251 (2013).
41. Steele, J. W. & Gandy, S. Apomorphine and Alzheimer A β : Roles for regulated α cleavage, autophagy, and antioxidation?. *Ann. Neurol.* **69**, 221–225 (2011).
42. Cheng, Z.-Y., Xia, Q.-P., Hu, Y.-H., Wang, C. & He, L. Dopamine D1 receptor agonist A-68930 ameliorates A β 1-42-induced cognitive impairment and neuroinflammation in mice. *Int. Immunopharmacol.* **88**, 106963 (2020).
43. Moreno-Castilla, P. et al. Dopaminergic neurotransmission dysfunction induced by amyloid- β transforms cortical long-term potentiation into long-term depression and produces memory impairment. *Neurobiol. Aging* **41**, 187–199 (2016).
44. Vorobyov, V. et al. Loss of midbrain dopamine neurons and altered apomorphine EEG effects in the 5x FAD mouse model of alzheimer’s disease. *JAD* **70**, 241–256 (2019).
45. Duzkiewicz, A. J., McNamara, C. G., Takeuchi, T. & Genzel, L. Novelty and dopaminergic modulation of memory persistence: a tale of two systems. *Trends Neurosci.* **42**, 102–114 (2019).
46. Schmalz, J. T. & Kumar, G. A computational model of dopaminergic modulation of hippocampal Schaffer collateral-CA1 long-term plasticity. *J. Comput. Neurosci.* **50**, 51–90 (2022).
47. Fucila, D., Domínguez-Álvaro, M., DeFelipe, J. & Alonso-Nanclares, L. Subregional density of neurons, neurofibrillary tangles and amyloid plaques in the hippocampus of patients with Alzheimer’s disease. *Front. Neuroanat.* **13**, 99 (2019).
48. Gloria, Y., Ceyzériat, K., Tsartsalis, S., Millet, P. & Tournier, B. B. Dopaminergic dysfunction in the 3xTg-AD mice model of Alzheimer’s disease. *Sci. Rep.* **11**, 19412 (2021).
49. Gasbarri, A., Packard, M. G., Campana, E. & Pacitti, C. Anterograde and retrograde tracing of projections from the ventral tegmental area to the hippocampal formation in the rat. *Brain Res. Bull.* **33**, 445–452 (1994).
50. Kempadoo, K. A., Mosharov, E. V., Choi, S. J., Sulzer, D. & Kandel, E. R. Dopamine release from the locus coeruleus to the dorsal hippocampus promotes spatial learning and memory. *Proc. Natl. Acad. Sci. Usa.* **113**, 14835–14840 (2016).
51. Sayegh, F. J. P. et al. Ventral tegmental area dopamine projections to the hippocampus trigger long-term potentiation and contextual learning. *Nat. Commun.* **15**, 4100 (2024).
52. Shohamy, D. & Adcock, R. A. Dopamine and adaptive memory. *Trends Cogn. Sci.* **14**, 464–472 (2010).
53. McNamara, C. G., Tejero-Cantero, Á., Trouche, S., Campo-Urriza, N. & Dupret, D. Dopaminergic neurons promote hippocampal reactivation and spatial memory persistence. *Nat. Neurosci.* **17**, 1658–1660 (2014).
54. Blanco-Duque, C., Chan, D., Kahn, M. C., Murdock, M. H. & Tsai, L. Audiovisual gamma stimulation for the treatment of neurodegeneration. *J. Intern. Med.* **295**, 146–170 (2024).
55. Iaccarino, H. F. et al. Gamma frequency entrainment attenuates amyloid load and modifies microglia. *Nature* **540**, 230–235 (2016).
56. Martorell, A. J. et al. Multi-sensory gamma stimulation ameliorates Alzheimer’s-associated pathology and improves cognition. *Cell* **177**, 256–271.e22 (2019).
57. Jones, M. et al. Gamma band light stimulation in human case studies: groundwork for potential alzheimer’s disease treatment. *JAD* **70**, 171–185 (2019).
58. Adaikkan, C. et al. Gamma entrainment binds higher-order brain regions and offers neuroprotection. *Neuron* **102**, 929–943.e8 (2019).
59. Lee, J. et al. 40 Hz acoustic stimulation decreases amyloid beta and modulates brain rhythms in a mouse model of Alzheimer’s disease. Preprint at <https://doi.org/10.1101/390302> (2018).
60. Chan, D. et al. Gamma frequency sensory stimulation in mild probable Alzheimer’s dementia patients: Results of feasibility and pilot studies. *PLoS ONE* **17**, e0278412 (2022).
61. McNett, S. D. et al. A feasibility study of AlzLife 40 Hz sensory therapy in patients with MCI and early AD. *Healthcare* **11**, 2040 (2023).
62. Cimenser, A. et al. Sensory-evoked 40-Hz gamma oscillation improves sleep and daily living activities in Alzheimer’s disease patients. *Front. Syst. Neurosci.* **15**, 746859 (2021).
63. Santarnecchi, E. et al. Individual differences and specificity of prefrontal gamma frequency-tACS on fluid intelligence capabilities. *Cortex* **75**, 33–43 (2016).
64. Santarnecchi, E. et al. Gamma tACS over the temporal lobe increases the occurrence of Eureka! moments. *Sci. Rep.* **9**, 5778 (2019).
65. Faltus, T., Freise, J., Fluck, C. & Zillmann, H. Ethics and regulation of neuronal optogenetics in the European Union. *Pflug. Arch. - Eur. J. Physiol.* **475**, 1505–1517 (2023).
66. Chen, R. et al. Deep brain optogenetics without intracranial surgery. *Nat. Biotechnol.* **39**, 161–164 (2021).
67. Banerjee, S., McCracken, S., Hossain, M. F. & Slaughter, G. Electrochemical detection of neurotransmitters. *Biosensors* **10**, 101 (2020).
68. Akyuz, E. et al. Revisiting the role of neurotransmitters in epilepsy: an updated review. *Life Sci.* **265**, 118826 (2021).
69. Bozzi, Y. & Borrelli, E. The role of dopamine signaling in epileptogenesis. *Front. Cell. Neurosci.* **7**, 157 (2013).
70. Lu, Y. et al. Electrodeposited polypyrrole/carbon nanotubes composite films electrodes for neural interfaces. *Biomaterials* **31**, 5169–5181 (2010).

71. Sekretaryova, A. N., Vagin, M. Y., Volkov, A. V., Zozoulenko, I. V. & Eriksson, M. Evaluation of the electrochemically active surface area of microelectrodes by capacitive and faradaic currents. *Chem-ElectroChem* **6**, 4411–4417 (2019).
72. Cogan, S. F. Neural stimulation and recording electrodes. *Annu. Rev. Biomed. Eng.* **10**, 275–309 (2008).
73. Xu, S. et al. An integrated system for synchronous detection of neuron spikes and dopamine activities in the striatum of Parkinson monkey brain. *J. Neurosci. Methods* **304**, 83–91 (2018).
74. Keith B.J. Franklin & George Paxinos. *Paxinos and Franklin's the Mouse Brain in Stereotaxic Coordinates, Compact: The Coronal Plates and Diagrams*. (Academic Press_RM, 2019).
75. Johnson, L. A. et al. Direct activation of primary motor cortex during subthalamic but not pallidal deep brain stimulation. *J. Neurosci.* **40**, 2166–2177 (2020).
76. Sloviter, R. S. Epileptic" brain damage in rats induced by sustained electrical stimulation of the perforant path. I. Acute electrophysiological and light microscopic studies. *Brain Res. Bull.* **10**, 675–697 (1983).

Acknowledgements

This work was sponsored by the National Natural Science Foundation of China (NSFC) (Nos. T2293730, T2293731, 62121003) and the Scientific Instrument Developing Project of the Chinese Academy of Sciences (CAS) (No. PTYQ2024BJ0009) to X.Cai, by NSFC (No. L2224042) and the Frontier Interdiscipline Project of the CAS (No. XK2022XXC003) to Y. Wu, by NSFC (No. 62333020) to Y. Song, by National Key Research and Development Program of China (NKRDP) (No. 2022YFC2402501) to M. Wang, by NSFC (No. 62171434) and the NKRDP (No. 2022YFB3205602) to J. Luo, by NSFC (No. 62471291), the Major Program of Scientific and Technical Innovation 2030 (No. 2021ZD02016030), the Joint Foundation Program of the CAS (No.8091A170201), and the National Natural Science Foundation of Beijing (No. F252069) to J. Liu.

Author contributions

S.L. and F.M. conceived the idea. S.L. and Z.X. designed and fabricated the electrodes. S.L., Yu.W. and Y.L. were responsible for electrode modification and material characterization. S.L., M.H. and Y.D. performed electrode implantation surgery. S.L., L.J., F.K. and Q.J. designed the electrical stimulation parameters. S. L., M. L., W. X. and P. J. conducted electrical stimulation modulation. S.L., M.W., J.L. and Jinping L. performed data analysis. S.L., J.W. and Z.F. participated in discussion and manuscript writing. Y. S., Y.W. and X.C. provided guidance and funding support.

Competing interests

S.L., X.C., Y.S., F.M., L.J., W.X. are involved in the patent 'Flexible Neural Electrode with Multilayer Bidirectional Signal Transmission Structure

and Its Fabrication Method'. The other authors declare no competing interests.

Ethics

All animal care and procedures adhered to the guidelines set by the Institutional Animal Care and Use Committee at the Aerospace Information Research Institute, Chinese Academy of Science (AIRCAS), and were approved by the Beijing Laboratory Animal Care Association and the AIRCAS Animal Care and Use Committee under approval number AIRCAS-202103-1.

Additional information

Supplementary information The online version contains supplementary material available at <https://doi.org/10.1038/s41467-025-60903-1>.

Correspondence and requests for materials should be addressed to Yilin Song, Yirong Wu or Xinxia Cai.

Peer review information *Nature Communications* thanks Alessandro Martorana, and the other, anonymous, reviewer(s) for their contribution to the peer review of this work. A peer review file is available.

Reprints and permissions information is available at <http://www.nature.com/reprints>

Publisher's note Springer Nature remains neutral with regard to jurisdictional claims in published maps and institutional affiliations.

Open Access This article is licensed under a Creative Commons Attribution-NonCommercial-NoDerivatives 4.0 International License, which permits any non-commercial use, sharing, distribution and reproduction in any medium or format, as long as you give appropriate credit to the original author(s) and the source, provide a link to the Creative Commons licence, and indicate if you modified the licensed material. You do not have permission under this licence to share adapted material derived from this article or parts of it. The images or other third party material in this article are included in the article's Creative Commons licence, unless indicated otherwise in a credit line to the material. If material is not included in the article's Creative Commons licence and your intended use is not permitted by statutory regulation or exceeds the permitted use, you will need to obtain permission directly from the copyright holder. To view a copy of this licence, visit <http://creativecommons.org/licenses/by-nc-nd/4.0/>.

© The Author(s) 2025